robotics

MDPI

Article

From Biological Gait to CPG Network Design: A Biomechanics-Driven Model-Selection Pipeline

Daniel Arriaga-Ventura [1], Riccardo Cespi [1], Javier Izquierdo [1], Stefano Di Gennaro [2] and Rogelio Bustamante-Bello [1,*]

[1] School of Engineering and Sciences, Instituto Tecnológico y de Estudios Superiores de Monterrey, Prolongación Canal de Miramontes 3855, Tlalpan, Ciudad de México 14386, Mexico; a01338696@tec.mx (D.A.-V.); rcespi@tec.mx (R.C.); jizquierdo.reyes@tec.mx (J.I.)

[2] Department of Information Engineering, Computer Science and Mathematics (DISIM), Università di L'Aquila, 67100 L'Aquila, Italy; stefano.digennaro@univaq.it

* Correspondence: rbustama@tec.mx

Abstract

Transferring observed gait coordination into executable Central Pattern Generator (CPG) specifications remains challenging because networks are often tuned empirically without systematic links to measured biomechanics. This study presents a biomechanics-driven pipeline using the walking gait of the fiddler crab *Uca pugnax*. Marker-based video analysis provided mean dominant frequency, movement amplitudes, phase relations, and coordination hierarchy. These descriptors defined oscillator roles, reference hierarchy, coupling topology, phase targets, communication direction, and an eight-oscillator architecture. A coarse-to-fine procedure selected parameters for phase-only Kuramoto and limit-cycle Hopf networks under unidirectional and bidirectional communication. Offline simulations assessed amplitude, phase-offset, convergence, dominant-frequency, and residual-oscillation errors. Kuramoto converged in 0.098 s under both communication schemes, with mean phase errors of 0.40% and 0.08%, respectively; both communication configurations preserved the prescribed gait frequency, with the bidirectional network producing 0.522 Hz. Hopf preserved frequency within 0.02% and 0.01%; the selected unidirectional configuration achieved the lower phase error, whereas the selected bidirectional configuration yielded a lower mean amplitude error (0.32% versus 2.87%), with longer convergence and residual oscillations. The pipeline provides a reproducible route from biological measurements to computational CPG design and model selection before physical deployment; robot validation is outside the present scope.

Keywords: Central Pattern Generators; bioinspired robotics; locomotion control; Kuramoto model; Hopf oscillator; biomechanics; gait analysis

Check for updates

Academic Editors: Yanhong Peng and Zhen Tian

Received: 18 September 2026
Revised: 16 October 2026
Accepted: 19 October 2026
Published: 22 October 2026

Copyright: © 2026 by the authors. Licensee MDPI, Basel, Switzerland. This article is an open access article distributed under the terms and conditions of the Creative Commons Attribution (CC BY) license.

1. Introduction

Reliable locomotion remains a persistent challenge in robotics. Controllers based on predefined trajectories or idealized analytical models can achieve precise motion under controlled conditions, yet their performance becomes harder to preserve when terrain, contact forces, or disturbances change. Animals confront these variations continuously by coordinating morphology, sensory information, and distributed motor activity rather than relying on a complete point-by-point motion plan. The highlighted differences make biological locomotion a rich source of applicable design ideas for improving adaptability, resilience to faults, and mobility in robotic systems [1–4].

A central feature of biological locomotion is its rhythmic organization. Walking, running, climbing, and swimming are produced through coordinated cycles that must remain stable while adapting to the environment. Central Pattern Generators (CPGs) capture this principle as compact neural circuits that generate rhythmic motor patterns while remaining responsive to sensory feedback and descending commands [3,5]. In robotics, CPGs can replace fully prescribed trajectories with a small set of oscillatory variables: intrinsic dynamics generate the rhythm, coupling terms establish inter-joint or inter-limb phase relations, and adjustable parameters shape frequency, amplitude, and coordination. This abstraction has supported locomotion in amphibious, salamander-like, snake-like, and undulatory robotic platforms [6–10].

Translating an observed gait into a CPG controller requires decisions about oscillator dynamics, connectivity, communication direction, and parameter selection. Reviews have examined these design challenges and the variety of available construction and optimization methods [3,4]. Related studies have compared oscillator formulations [11], evaluated alternative CPG topologies [12], and proposed transparent oscillator parameterizations [13]. More recently, Almeida and Santos [14] identified parameter tuning and the need for consistent validation protocols as continuing challenges in control based on CPGs and dynamic movement primitives (DMPs) for wearable lower-limb robots. Together, these studies motivate explicit documentation of how biological measurements and engineering choices determine a CPG specification and the conditions used to compare alternative formulations. Accordingly, this study asks how biological gait descriptors can be translated into an executable and reproducible CPG network through explicit design and parameter-selection steps that also support comparisons under common targets and evaluation criteria.

To answer this question, this work introduces a pipeline that organizes the transition from biological observation to computational CPG network design for robotic applications into Biological Analysis, Signal Processing, and CPG Implementation. The walking gait of *Uca pugnax* serves as the case study. Its mean dominant frequency, movement amplitudes, phase offsets, motion-unit roles, and coordination relations are used, together with robotic actuation constraints, to define oscillator assignments, a reference hierarchy, connectivity, and phase-target matrices. This process yields an executable eight-oscillator specification composed of four primary units representing proximal limb motion and four associated units representing distal limb motion.

The methodological contribution is the explicit connection between biological-to-network translation, parameter selection, and model evaluation within one traceable workflow. The pipeline distinguishes measured biological targets and structural choices informed by gait coordination and robotic actuation from the coupling gains and Hopf limit-cycle radius selected through multi-resolution grid search (MRGS). This makes the basis of network construction and parameter selection inspectable and provides a shared specification for evaluating established oscillator formulations [11,15,16]. Kuramoto and Hopf networks are implemented computationally using the same mean biological targets and connectivity specifications for each communication condition, and evaluated through offline simulation under unidirectional and bidirectional communication. The resulting model-selection guidelines relate phase accuracy, amplitude tracking, convergence, and frequency error to the requirements established by the biological-to-CPG translation and are restricted to the formulations and conditions evaluated in this study.

The main contributions of this work are as follows.

- We establish a traceable biological-to-CPG network-design pipeline organized into Biological Analysis, Signal Processing, and CPG Implementation.
- We demonstrate in simulation how measured gait descriptors can be transformed into an executable eight-oscillator CPG architecture that preserves the distinction between

proximal and distal limb motions, together with the reference hierarchy, topology, and target phase relations identified for *Uca pugnax*.

- We perform a controlled comparison of Kuramoto and Hopf networks using common mean biological targets, network specifications, communication schemes, and evaluation metrics, with the parameters of each configuration selected independently by MRGS.
- We derive implementation-oriented model-selection guidelines from amplitude tracking, phase accuracy, convergence time, dominant-frequency error, residual phase behavior, and optimization complexity.

Figure 1 summarizes the proposed methodology and its connection between biological observation, signal processing, and CPG network design intended for robotic locomotion applications.

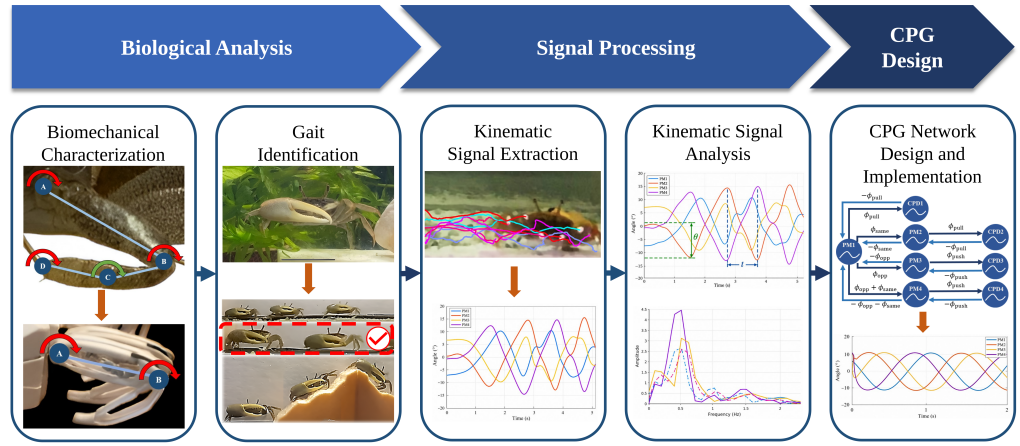


Figure 1. Proposed methodology for translating biological gait into computational CPG network design for robotic locomotion applications. Blue arrows indicate the workflow between the main methodological blocks, while orange arrows indicate the results obtained at each step. Curved arrows represent rotational motion at the corresponding joints, with their colors indicating the associated rotation axes relative to the reference coordinate system shown in each image. In the kinematic signal analysis, the green θ annotation represents the angular amplitude, while the blue t annotation indicates the signal period. The red dashed box and check mark identify the gait selected for subsequent kinematic analysis and CPG implementation.

2. Background

CPGs are compact neural circuits that generate periodic activity for rhythmic motor behaviors such as walking, swimming, running, and breathing [3,5]. Their key feature is local rhythm generation: coordinated motion can be produced without a high-level command specifying every instant of the cycle, while sensory feedback and descending modulation can still adjust the pattern. For engineering, this is useful because rhythmic control can be represented as a low-dimensional dynamical process. Cadence and inter-limb coordination can then be modulated without prescribing a fully time-indexed joint trajectory [4,10].

Robotic CPG controllers are often implemented using either spiking neural networks (SNNs) or coupled-oscillator networks [4,13]. SNNs are useful when the model is intended to preserve some of the neuronal dynamics involved in rhythm generation. They can also capture nonlinear interactions among connected units. This level of detail comes with a practical cost. Implementing the model requires decisions about the network architecture, synaptic weights, and neuronal time constants. The relation between excitatory and inhibitory activity must also be defined. Consequently, obtaining stable behavior is not

always straightforward, and a parameter set that works in one experiment may be difficult to reproduce under different conditions [13].

Coupled-oscillator networks describe rhythmic coordination through a more compact set of variables. Each oscillator is generally defined by its intrinsic frequency, while the coordination among units is established through phase relationships and coupling terms. These variables can be related directly to measurable gait characteristics, such as the dominant movement frequency and the phase offsets between limbs. The resulting controller can therefore be examined in terms of frequency, phase, coupling strength, and network topology [3,6,9]. Coupling gains must nevertheless be selected for the target coordination pattern and the chosen network configuration. Previous work addresses such decisions through several design and optimization approaches [4,17].

Previous work provides structured approaches to CPG construction and learning. Yu et al. [4] reviewed model design, optimization, and implementation strategies. Espinal et al. [17] used Christiansen Grammar Evolution to select spiking-network connectivity and synaptic weights for reproducing insect-inspired gait patterns in a hexapod robot. Li et al. [18] combined imitation learning of rhythmic feedforward patterns with reinforcement learning of a reflex neural network for bipedal locomotion. Building on these antecedents, the present study develops an explicit sequence from measured gait descriptors and robotic actuation constraints to oscillator roles, a reference hierarchy, connectivity, and phase targets. It then links that specification to MRGS-based parameter selection and comparison of Kuramoto and Hopf networks using shared biological targets and evaluation metrics.

The following subsections introduce the two coupled-oscillator formulations used here and identify the design choices that must be fixed before a fair comparison is possible. The discussion focuses on how frequency targets, phase relations, coupling structure, and network topology are represented in Kuramoto and Hopf networks. These elements form the shared vocabulary used later to move from biological measurements to an executable CPG.

2.1. Kuramoto Model

The Kuramoto model is used in this study as a reference for phase coordination in coupled-oscillator CPGs [15]. Its formulation describes coordination through the phases of the oscillators and the gains that couple them. This is convenient for locomotion studies because the desired timing between limbs can be expressed directly as phase differences. Kuramoto-based networks have therefore been used in robotic systems to establish gait timing and coordinate the motion of multiple limbs [3,13].

Consider a network composed of N oscillators. Oscillator i is described by its phase θ_i and its intrinsic frequency f_i. The parameter K_{ij} defines the influence of oscillator j on oscillator i. Thus, the phase of each oscillator changes according to its own frequency and the phase differences with the other units in the network. In the classical Kuramoto formulation, this behavior is written as [15]

$$\dot{\theta}_i = 2\pi f_i + \sum_{j=1}^{N} K_{ij} \sin(\theta_j - \theta_i), \qquad i = 1, \ldots, N. \tag{1}$$

The sinusoidal coupling term tends to reduce or maintain the phase differences between connected oscillators, depending on the selected gains and the desired coordination pattern. As a result, synchronized behavior can arise from interactions defined locally between the units rather than from a complete time-indexed trajectory.

Some CPG implementations extend the Kuramoto model by including amplitude states and relaxation dynamics. These extensions allow frequency, phase, and amplitude

to be modified independently, which is useful when the gait amplitude must change during operation [4,12]. In this work, however, only the phase dynamics are implemented. The output amplitude is fixed through an external scaling factor, so no additional amplitude-state equation is required. The specific equations and parameters used in the simulations are presented in the CPG Implementation stage.

2.2. Hopf Model

The Hopf oscillator is included as a limit-cycle model grounded in bifurcation theory, where a stable equilibrium loses stability and a self-sustained periodic orbit emerges. This property makes the Hopf formulation well suited for rhythmic pattern generation in CPG settings because oscillations are inherently stable and can be modulated through a small set of parameters that shape amplitude, frequency, and coupling-driven coordination across units [11,16].

A commonly used planar Hopf oscillator is defined by two state variables, u and v, whose joint dynamics converge to a limit cycle. In a standard parameterization, the oscillation amplitude is regulated by the limit-cycle radius, while the intrinsic frequency is set by a frequency parameter. One convenient form is

$$\dot{u} = \kappa\Big(R^2 - (u^2 + v^2)\Big)u - 2\pi f\, v, \qquad \dot{v} = \kappa\Big(R^2 - (u^2 + v^2)\Big)v + 2\pi f\, u, \tag{2}$$

where R determines the target oscillation magnitude, f sets the intrinsic frequency, and κ controls how quickly the state converges to the limit cycle.

For multi-oscillator CPGs, coupling terms are added to the planar dynamics to impose coordination and desired phase relationships across the network [3,11]. The form of this coupling depends on the selected topology, phase convention, and output mapping; therefore, the exact network equations used in this study are presented in the CPG Implementation stage rather than through an additional generic example here. Because the origin is an equilibrium of the uncoupled Hopf oscillator, a nonzero initial perturbation is required to initiate the periodic response.

3. Methodology

The methodology translates biological locomotion into an executable CPG network through five sequential stages grouped into Biological Analysis, Signal Processing, and CPG Implementation. First, biomechanical characterization identifies the biological joints corresponding to the available robotic actuation, and gait identification selects the locomotion pattern to be reproduced. Kinematic signal extraction and analysis then provide the movement amplitudes, dominant frequency, and phase relationships required for CPG synthesis. Finally, these descriptors are used to assign oscillator roles, define the coupling topology and phase targets, and parameterize the Kuramoto and Hopf networks. The following subsections describe each stage for the *Uca pugnax* case study.

3.1. Biomechanical Characterization

The development of a CPG-based locomotion controller requires a correspondence between the motion of the biological limbs and the available actuation of the robotic platform. For this reason, the biomechanical analysis first identifies the relevant degrees of freedom in the biological model. These degrees of freedom are then compared with the joints that can be actuated in the robot. The comparison establishes which anatomical joints should be tracked during the kinematic analysis and, subsequently, which signals will be used to characterize the gait.

An adult specimen preserved in a 10% saline solution was used for the biomechanical characterization. The solution maintained sufficient joint mobility to manipulate the

limbs and examine their rotation axes. Four rotational joints were identified in each leg: carapace–merus, merus–carpus, carpus–propodus, and propodus–dactylus, as illustrated in Figure 2. The rotation axes of the carapace–merus, merus–carpus, and propodus–dactylus joints are approximately aligned. In contrast, the axis of the carpus–propodus joint is oriented orthogonally, allowing the limb to change its direction of motion. Since the specimen has four legs on each side of its body, the complete set of lower limbs contains 32 rotational joints.

The robotic platform, however, provides only eight actuated degrees of freedom. Two motors drive each interleaved leg pair, corresponding to the carapace–merus and merus–carpus joints shown in Figure 2. The kinematic analysis was therefore restricted to these two joints, since they provide the direct correspondence between the biological motion and the available robot actuation. For each interleaved pair, only one biological leg was analyzed. Its paired leg was not treated independently because both legs are driven together and reproduce the same commanded motion in the robotic platform.

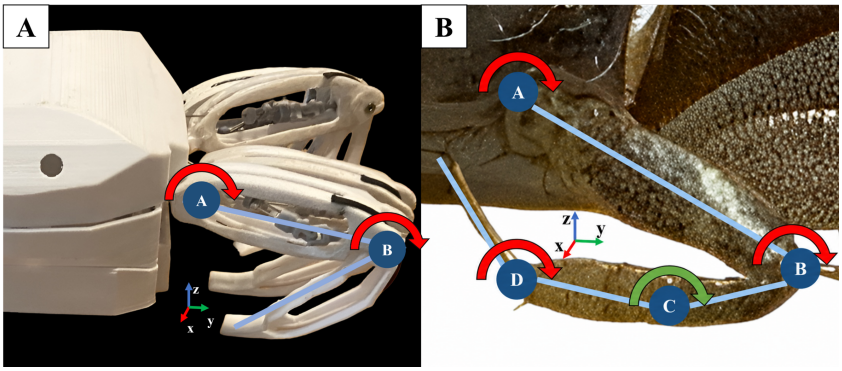


Figure 2. (**A**) Robotic platform joint layout: carapace–merus (A) and merus–carpus (B). (**B**) *Uca pugnax* leg joint schematic: carapace–merus (A), merus–carpus (B), carpus–propodus (C), and propodus–dactylus (D). The curved arrows indicate rotational motion at the corresponding joints, with their colors identifying the associated rotation axes according to the reference coordinate systems shown in each panel.

3.2. Gait Identification

After identifying the anatomical joints relevant to the robotic platform, the next step was to select the locomotion pattern to be reproduced. This stage was conducted as a qualitative behavioral screening rather than as a quantitative occurrence study. The available gaits were not defined in advance; instead, the observed locomotion patterns were distinguished according to their limb coordination, qualitative movement characteristics, and behavioral context. The purpose of this screening was to identify a suitable reference gait for the subsequent periodic kinematic analysis and CPG implementation.

Eight adult male *Uca pugnax* specimens ($n = 8$) were included in the qualitative screening. They were housed in a $20 \times 40 \times 30$ cm aquarium containing wet and dry zones representative of an intertidal environment. The habitat included natural substrate, a burrow, aquatic vegetation (*Echinodorus amazonicus* and *Elodea canadensis*), and full-spectrum illumination. Reflective film was placed around the aquarium to reduce external visual disturbances. Locomotion was recorded from frontal and lateral views to examine limb coordination and identify the behavioral context associated with each locomotion pattern. The number of occurrences of each gait was not systematically counted; therefore, this stage does not support quantitative comparisons of gait frequency, prevalence, or repeatability across specimens.

The qualitative screening identified three locomotion patterns: walking, running, and climbing, all characterized by alternating lower-limb coordination. Walking occurred

during spontaneous routine displacement and foraging and exhibited comparatively low-frequency, small-amplitude movements. Running preserved the same alternating coordination but involved higher-frequency and larger-amplitude motions, typically associated with external disturbances. Climbing occurred during obstacle negotiation and depended strongly on obstacle geometry and surface contact, as illustrated in Figure 3.



Figure 3. Locomotion patterns observed in *Uca pugnax*: running (**A**), walking (**B**), and climbing (**C**).

Walking was selected as the reference gait because it provided a spontaneous and periodic locomotion pattern that could be recorded without introducing an external disturbance or obstacle. This allowed its dominant frequency, movement amplitudes, and inter-limb phase relationships to be characterized under consistent recording conditions. The selection was qualitative and was not based on quantified gait occurrence or statistical repeatability.

3.3. Kinematic Signal Extraction

This stage converts the limb movements selected in Section 3.2 into time-dependent kinematic signals. The positions of the relevant limb segments are obtained from video recordings and used to reconstruct their angular or linear trajectories. These signals provide the locomotor descriptors required for gait imitation, including dominant frequency, movement amplitude, and phase offsets between limbs. A video-tracking procedure is therefore used to follow the position of the selected anatomical points throughout each recording.

A separate group of four adult male specimens ($n = 4$) was used for the subsequent quantitative kinematic analysis. Approximately 2-mm-diameter markers were painted on the exoskeleton using non-toxic white paint to provide high contrast during video processing. For each analyzed limb, one marker was located at the carapace–merus joint and another at the joint between the merus and carpus. A third marker was positioned at the distal endpoint of the carpus–propodus–dactylus (CPD) segment. The tracked position corresponded to the approximate center of each marker, and the three coordinates defined the geometry used to reconstruct the merus and distal CPD trajectories.

All specimens were obtained from a captive breeder, without collection from the wild. They were maintained in an aquarium providing access to moist and dry areas, a fine-sand substrate, and hiding places. The aquarium contained aquatic plants (*Echinodorus amazonicus* and *Elodea canadensis*) and aquarium snails, and was equipped with a filtration pump. A full-spectrum lamp rated at 60 W was positioned approximately 50 cm above the water surface. Commercial flake food formulated for aquatic animals was provided. Visual barriers were installed along the aquarium sides to reduce exposure to external visual stimuli. Experimental handling and recording sessions were limited in duration with the aim of minimizing disturbance.

Videos were recorded with an iPhone 11 in horizontal orientation under uniform white illumination. The camera remained fixed on a tripod throughout each trial, digital zoom and changes in magnification were disabled, and the camera–specimen distance was approximately 15 cm. Before upload to Google Drive, the recordings were spatially cropped to retain the aquarium region containing the observed locomotion. This region extended from the aquarium base to the water level and covered approximately 30 cm horizontally and 7.44 cm vertically. The cropped files were transferred through Google Drive without additional compression and subsequently imported into Tracker for kinematic analysis. Tracker's video properties reported frame dimensions of 1916 × 476 pixels and a frame rate of 30 fps, corresponding to the sampling period

$$T_s = \frac{1}{30} \approx 0.033 \text{ s}.$$

An internal glass partition was positioned 5 cm from the front wall of the aquarium and extended to approximately half the aquarium height. The partition restricted the crab's movement to a corridor approximately parallel to the front wall. The camera image plane was maintained approximately parallel to these glass surfaces. This controlled geometry favored displacement approximately parallel to the image plane; only sequences that satisfied this geometry and were appropriate for two-dimensional kinematic analysis were retained.

A reference ruler was positioned immediately adjacent to the specimen displacement plane. The ruler plane and the specimen motion plane were separated by approximately 4 mm, corresponding to the thickness of the aquarium glass, rather than being assumed to coincide exactly. Each recording was individually subjected to spatial scale calibration in Tracker. The Tracker Calibration Stick was positioned between two ruler marks separated by exactly 1 cm, and this length was entered to establish the pixel-to-length scale for that video. This procedure was a spatial calibration using a reference ruler; no optical calibration of the intrinsic or extrinsic camera parameters was performed. The marker arrangement used for kinematic tracking is shown in Figure 4.

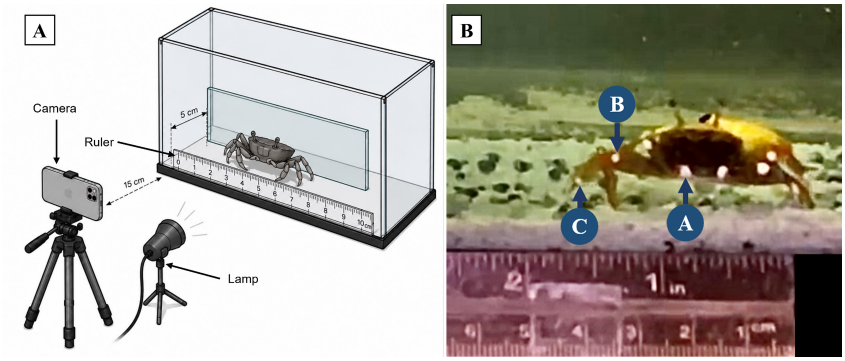


Figure 4. Experimental acquisition and marker-tracking configuration: (**A**) AI-generated schematic of the recording setup; (**B**) representative frame showing markers at the carapace–merus joint (A), merus–carpus joint (B), and distal CPD endpoint (C).

Four video trials were recorded for each specimen. Each recording selected for quantitative analysis contained a continuous 8 s interval of spontaneous locomotion without evident interruptions. Before coordinate extraction, the illumination, marker contrast, and template-matching conditions were assessed using the match coincidence percentage provided by Tracker. Marker coordinates were then obtained through a combined procedure: AutoTracker was used while a marker remained clearly visible, and manual correction or manual digitization was applied within the same track in frames where a limb temporarily occluded the marker or prevented reliable automatic identification.

The manual intervention therefore corrected losses of automatic tracking caused by occlusion rather than constituting a separate measurement method. The resulting coordinates were converted into the kinematic signals presented in Figure 5.

Previous Tracker-based video analysis reports a conservative localization uncertainty of approximately ±2 pixels for clearly visible objects under appropriate acquisition conditions [19]. For the representative image scale used in this study, this corresponds to approximately ±0.32 mm. This value is reported as a representative system-level localization estimate, while each recording was individually calibrated using the reference ruler. It was not propagated into an angular uncertainty or incorporated into the CPG target parameters.

The acquisition remains subject to the limitations of two-dimensional kinematic analysis, including small out-of-plane motions, the approximately 4-mm separation between the ruler and specimen planes, manual corrections during marker occlusion, and the absence of an independent intra-operator repeatability assessment. These effects were mitigated through fixed camera geometry, approximately parallel motion and image planes, individual spatial calibration, high-contrast markers, and selection of recordings suitable for two-dimensional tracking.

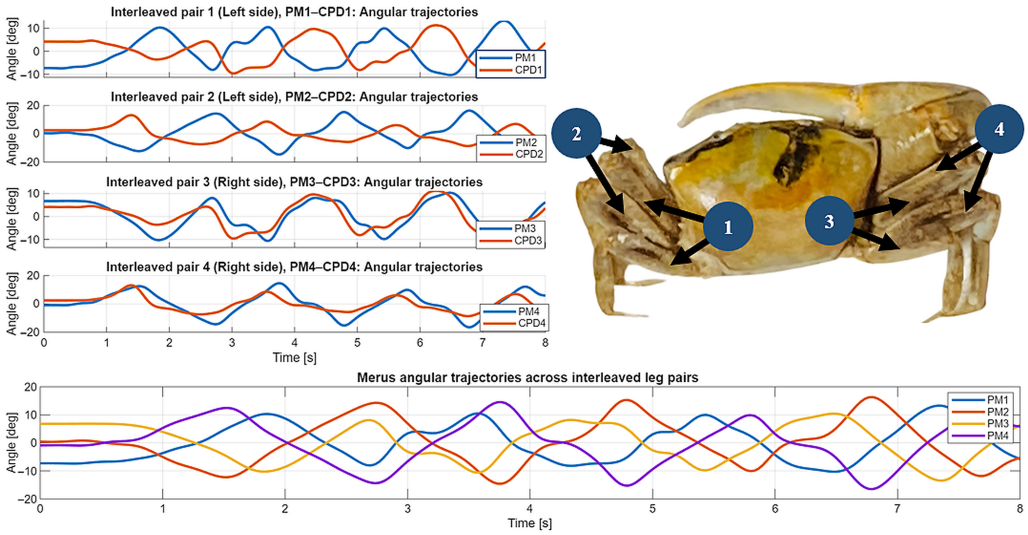


Figure 5. Angular trajectories of the Pair of Merus (PM) and carpus–propodus–dactylus (CPD) segments during walking gait. The adjacent panel indicates the interleaved leg pairs, 1–4.

The experimental-setup schematic in Figure 4A was generated using the image-generation function of ChatGPT (OpenAI). The input comprised an author-provided hand-drawn sketch of the actual experimental setup and a written description of its experimental parameters. A formal, subdued visual style was requested. The generated diagram was refined through iterative prompts to correct the distance annotations between setup components and remove unwanted automatically generated labels. The final element labels were added manually in Microsoft PowerPoint (Microsoft). The authors reviewed the schematic for consistency with the experimental arrangement. The figure serves as an illustrative representation of the setup; quantitative measurements were obtained from the experimental video recordings and their analysis in Tracker.

3.4. Kinematic Signal Analysis

The extracted angular trajectories were analyzed to obtain the gait descriptors required for CPG design: dominant frequency, movement amplitude, and phase relationships. PM and CPD amplitudes were measured during steady locomotion, while the dominant frequency was identified from the frequency spectrum as the fundamental component

with the largest magnitude. Phase relationships were evaluated between PM signals from different limbs and between the PM and CPD segments within each limb.

Before phase-delay estimation, the angular trajectories were visually inspected to select common 8 s analysis windows for the signals being compared, containing regular movement cycles without visually apparent modulation. Each window encompassed approximately four gait cycles. Outliers were identified using a moving-median criterion with a 0.5 s window and a threshold factor of 3. Flagged values were replaced using piecewise cubic Hermite interpolation (PCHIP), followed by nearest-neighbor filling for remaining missing values. The trajectories were then filtered using a fourth-order Butterworth low-pass filter with a 3 Hz cutoff, applied forward and backward through MATLAB R2025a's `filtfilt` function. Each trajectory was centered by subtracting its mean to remove the DC component. No additional linear detrending or amplitude normalization was applied.

Relative delays between pairs of preprocessed angular trajectories were subsequently estimated using MATLAB's `finddelay` function, which returns the delay in samples between two sequences. Each delay was converted to time using the sampling period of approximately 0.033 s and then converted to phase, in degrees, by multiplying it by the corresponding dominant movement frequency and by 360.

Four trials were analyzed for each of the four crab specimens. The trial-level estimates were first averaged within each specimen to obtain one specimen-level value for each descriptor. The global mean and the between-specimen standard deviation were then calculated across the four specimen-level means ($n = 4$). The same specimen-level procedure was applied to the PM and CPD amplitudes and to the derived pushing-phase descriptor ϕ_{push}. Thus, the 16 recordings were treated as repeated trials rather than as 16 independent biological samples. The resulting mean gait descriptors and their between-specimen variability are reported in Table 1.

Table 1. Walking-gait descriptors reported as mean ± between-specimen standard deviation, based on four specimens ($n = 4$).

Dominant Frequency	**Phase Offsets**				**Amplitudes**	
f_n	ϕ_{same}	ϕ_{opp}	ϕ_{pull}	ϕ_{push}	A_{PM}	A_{CPD}
0.522 ± 0.001 Hz	$119.3 \pm 0.45^\circ$	$179.1 \pm 0.38^\circ$	$90.5 \pm 0.23^\circ$	$271.3 \pm 0.31^\circ$	$13.7 \pm 1.8^\circ$	$11.1 \pm 1.6^\circ$

3.5. CPG Network Design

The CPG network design comprises oscillator assignment, coupling-topology definition, and model parameterization. Oscillators are classified as independent when they provide a primary timing reference and as dependent when their phase is defined relative to an independent unit. In the case study, each interleaved leg pair is represented by an independent PM oscillator and a dependent CPD oscillator, yielding four PM and four CPD units. Based on the gait analysis in Sections 3.3 and 3.4, PM1 was selected as the zero-phase reference. The remaining PM oscillators were coupled to PM1, while each CPD oscillator remained linked to its corresponding PM unit. Figure 6 summarizes the resulting architecture.

Two communication schemes were considered under the same target connectivity: unidirectional and bidirectional coupling. Unidirectional coupling propagates information from a source oscillator to a receiving oscillator, whereas bidirectional coupling introduces reciprocal interaction between connected units. The corresponding network topologies are shown in Figure 6.

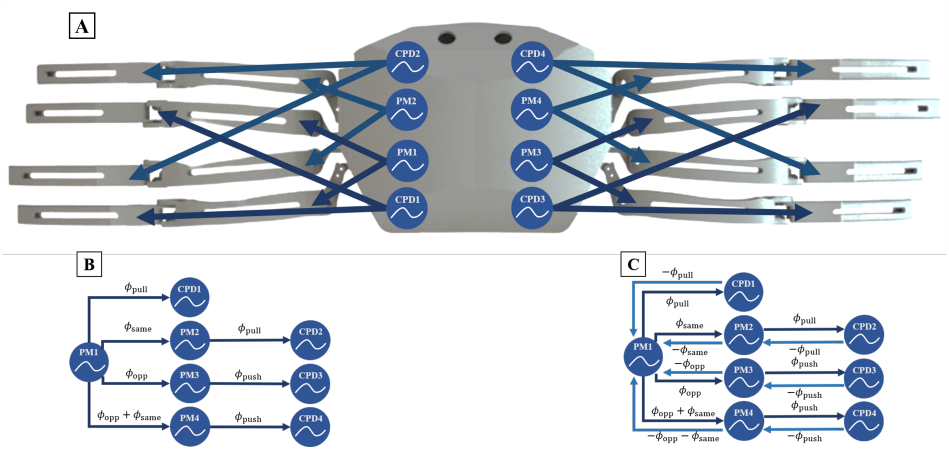


Figure 6. CPG architecture used in the case study: (**A**) distribution of PM and CPD oscillators across the four interleaved leg pairs of the robotic platform; (**B**) unidirectional coupling topology; and (**C**) bidirectional coupling topology. The arrows in (**A**) indicate the assignment of oscillator outputs to the corresponding robotic leg elements, whereas those in (**B**,**C**) indicate the direction of coupling between oscillators, with labels specifying the target phase offsets.

After the network map and its communication alternatives have been defined, the next step is to formulate the corresponding topology matrix. This matrix provides the mathematical representation that translates the graphical CPG network into the coupling structure used by the oscillator models. For both rows and columns, the oscillators are ordered as

$$\mathcal{O} = [\mathrm{PM}_1, \mathrm{PM}_2, \mathrm{PM}_3, \mathrm{PM}_4, \mathrm{CPD}_1, \mathrm{CPD}_2, \mathrm{CPD}_3, \mathrm{CPD}_4]. \tag{3}$$

Under the adopted convention, columns represent emitting oscillators and rows represent receiving oscillators. Thus, $T_{ij} = 1$ indicates a direct coupling from oscillator j to oscillator i, whereas $T_{ij} = 0$ indicates no direct connection. The resulting unidirectional and bidirectional topology matrices are given in Equations (4) and (5), respectively.

$$\mathbf{T}_{\text{uni}} = \begin{bmatrix} 0 & 0 & 0 & 0 & 0 & 0 & 0 & 0 \\ 1 & 0 & 0 & 0 & 0 & 0 & 0 & 0 \\ 1 & 0 & 0 & 0 & 0 & 0 & 0 & 0 \\ 1 & 0 & 0 & 0 & 0 & 0 & 0 & 0 \\ 1 & 0 & 0 & 0 & 0 & 0 & 0 & 0 \\ 0 & 1 & 0 & 0 & 0 & 0 & 0 & 0 \\ 0 & 0 & 1 & 0 & 0 & 0 & 0 & 0 \\ 0 & 0 & 0 & 1 & 0 & 0 & 0 & 0 \end{bmatrix} \tag{4}$$

$$\mathbf{T}_{\text{bi}} = \begin{bmatrix} 0 & 1 & 1 & 1 & 1 & 0 & 0 & 0 \\ 1 & 0 & 0 & 0 & 0 & 1 & 0 & 0 \\ 1 & 0 & 0 & 0 & 0 & 0 & 1 & 0 \\ 1 & 0 & 0 & 0 & 0 & 0 & 0 & 1 \\ 1 & 0 & 0 & 0 & 0 & 0 & 0 & 0 \\ 0 & 1 & 0 & 0 & 0 & 0 & 0 & 0 \\ 0 & 0 & 1 & 0 & 0 & 0 & 0 & 0 \\ 0 & 0 & 0 & 1 & 0 & 0 & 0 & 0 \end{bmatrix} \tag{5}$$

The phase-offset matrices follow the same sparsity pattern as the corresponding topology matrices. Each nonzero entry defines the target phase relation of an active

coupling, while reciprocal links use the opposite sign to preserve the same relative phase difference. The resulting matrices are given in Equations (6) and (7).

$$\boldsymbol{\phi}_{\text{uni}} = \begin{bmatrix} 0 & 0 & 0 & 0 & 0 & 0 & 0 & 0 \\ \phi_{\text{same}} & 0 & 0 & 0 & 0 & 0 & 0 & 0 \\ \phi_{\text{opp}} & 0 & 0 & 0 & 0 & 0 & 0 & 0 \\ \phi_{\text{opp}} + \phi_{\text{same}} & 0 & 0 & 0 & 0 & 0 & 0 & 0 \\ \phi_{\text{pull}} & 0 & 0 & 0 & 0 & 0 & 0 & 0 \\ 0 & \phi_{\text{pull}} & 0 & 0 & 0 & 0 & 0 & 0 \\ 0 & 0 & \phi_{\text{push}} & 0 & 0 & 0 & 0 & 0 \\ 0 & 0 & 0 & \phi_{\text{push}} & 0 & 0 & 0 & 0 \end{bmatrix} \tag{6}$$

$$\boldsymbol{\phi}_{\text{bi}} = \begin{bmatrix} 0 & -\phi_{\text{same}} & -\phi_{\text{opp}} & -\phi_{\text{opp}} - \phi_{\text{same}} & -\phi_{\text{pull}} & 0 & 0 & 0 \\ \phi_{\text{same}} & 0 & 0 & 0 & 0 & -\phi_{\text{pull}} & 0 & 0 \\ \phi_{\text{opp}} & 0 & 0 & 0 & 0 & 0 & -\phi_{\text{push}} & 0 \\ \phi_{\text{opp}} + \phi_{\text{same}} & 0 & 0 & 0 & 0 & 0 & 0 & -\phi_{\text{push}} \\ \phi_{\text{pull}} & 0 & 0 & 0 & 0 & 0 & 0 & 0 \\ 0 & \phi_{\text{pull}} & 0 & 0 & 0 & 0 & 0 & 0 \\ 0 & 0 & \phi_{\text{push}} & 0 & 0 & 0 & 0 & 0 \\ 0 & 0 & 0 & \phi_{\text{push}} & 0 & 0 & 0 & 0 \end{bmatrix} \tag{7}$$

The mean gait descriptors in Table 1 were adopted as common targets for both CPG formulations. The intrinsic oscillator frequency was set to $f = 0.522$ Hz from the measured biological dominant frequency f_n. Between-specimen standard deviations were retained as descriptors of biological variability and were not incorporated into the controller equations, optimization objectives, or target parameters.

Using these common targets, the Kuramoto and Hopf networks were implemented according to Equations (8)–(12). The Kuramoto network uses the phase state θ_i and coupling gain ω, whereas the Hopf network uses the state pair (u_i, v_i), with $\kappa = 1$ and a common limit-cycle radius $R_i = R$. Accordingly, MRGS selects ω for Kuramoto and (R, ϵ) for Hopf, while topology, phase targets, intrinsic frequency, and output amplitudes remain fixed.

$$\dot{\theta}_i = 2\pi f + \omega \sum_{j=1}^{N} T_{ij} \sin(\theta_j - \theta_i - \phi_{ij}), \qquad i = 1, \ldots, N. \tag{8}$$

$$x_i(t) = A_i \cos(\theta_i(t)). \tag{9}$$

$$\dot{u}_i = \kappa\left(R_i^2 - u_i^2 - v_i^2\right) u_i - 2\pi f\, v_i, \qquad i = 1, \ldots, N. \tag{10}$$

$$\begin{aligned} \dot{v}_i = {} & \kappa\left(R_i^2 - u_i^2 - v_i^2\right) v_i + 2\pi f\, u_i \\ & + \epsilon \sum_{j=1}^{N} T_{ij} \Big(- u_j \sin(\phi_{ij}) + v_j \cos(\phi_{ij}) \Big), \qquad i = 1, \ldots, N. \end{aligned} \tag{11}$$

$$x_i(t) = \frac{A_i}{R_i} u_i(t). \tag{12}$$

Following the ordering in $\mathcal{O}$, the output amplitudes were set to $A_i = A_{\text{PM}}$ for $i = 1, \ldots, 4$ and $A_i = A_{\text{CPD}}$ for $i = 5, \ldots, 8$, using the targets in Table 1.

Kuramoto coupling gains were selected independently for the unidirectional and bidirectional networks using a multi-resolution grid search (MRGS). The initial domain was $0 \leq \omega \leq 100$, with successive step sizes of 10, 1, 0.1, and 0.01. At each level, the search

interval was refined using the neighboring grid points surrounding the selected candidate, retaining the domain boundary when the candidate occurred at an endpoint. Each candidate was evaluated over 8 s using simultaneous forward-Euler updates with $\Delta t = 0.002$ s and initial phases $\theta_i(0) = 0$.

The objective was to minimize the phase-convergence time t_c, defined as the first sample initiating N_h consecutive samples for which the maximum absolute wrapped phase error across all active couplings remained within $\delta = 5^\circ$. The sample count was $N_h = \max\{1, \text{round}(\tau_h/\Delta t)\}$, with the nominal persistence setting $\tau_h = 0.05$ s. Candidates that did not satisfy this criterion within the simulation horizon were discarded. Ties were resolved by retaining the first candidate in ascending gain order. The resulting gains were $\omega_{\text{uni}} = 99.29$ and $\omega_{\text{bi}} = 99.28$. These values represent selections within the evaluated grids and numerical resolution and do not establish a unique or global optimum.

Hopf parameters were selected independently for the unidirectional and bidirectional networks using a nested MRGS over the common limit-cycle radius R and coupling gain ϵ, with $\kappa = 1$. The initial domains were $0.1 \leq R \leq 10$ and $0 \leq \epsilon \leq 2$, refined using step sizes of 0.5, 0.1, and 0.01 for R, and 0.1, 0.01, and 0.001 for ϵ. Upper bounds could be expanded to $R = 50$ and $\epsilon = 10$ when the best candidate occurred at the initial boundary.

For each candidate radius, ϵ was selected to minimize convergence time while maintaining a mean output-amplitude error below 3%; otherwise, the candidate with the lowest mean amplitude error was retained. Unstable solutions or cases that failed the phase-convergence criterion were discarded. The selected parameter pairs were $(R, \epsilon) = (1.83, 1.19)$ for the unidirectional network and $(2.86, 0.55)$ for the bidirectional network. For the latter, several candidates around $\epsilon = 0.50$–0.55 satisfied the selection criteria, with $\epsilon = 0.55$ providing the lowest convergence time among the evaluated candidates. These parameters represent the best-performing solutions within the evaluated domains and resolutions and do not establish global optimality.

Initial-condition sensitivity was evaluated while keeping the selected network parameters and biological targets fixed. For each communication scheme, 50 independent phase-deviation vectors were sampled uniformly from $[-\pi/6, \pi/6]$ and another 50 from $[-\pi, \pi]$. The same recorded deviations were used across models and communication schemes. Kuramoto initial phases were $\theta_i(0) = \Delta_i$. Hopf initial states were $u_i(0) = -r_i(0)\sin\Delta_i$ and $v_i(0) = r_i(0)\cos\Delta_i$, with $r_i(0) = 0.1$ for the phase-only variations. An additional 50 Hopf trials reused the wider phase deviations with independently sampled initial radii $r_i(0) \in [0.05, 0.15]$. This produced 100 randomized trials per Kuramoto configuration and 150 per Hopf configuration, without parameter retuning. The nominal initializations and an all-zero Hopf initialization were examined separately.

All trials used simultaneous forward-Euler integration with $\Delta t = 0.002$ s over 120 s. The phase-band criterion defined above was applied to both models, recording first entry and subsequent band retention separately. Additional diagnostics were evaluated over a common final window of 90–120 s: mean absolute wrapped phase error across the seven biological phase relations, output-amplitude error estimated from the half peak-to-peak range, and frequency estimated from the slope of unwrapped phase. Their changes were calculated relative to the nominal trial of the same configuration. Trials that did not satisfy the phase-band criterion within the simulation horizon remained included in the reported counts. The all-zero Hopf diagnostic was excluded from the randomized-trial summaries.

4. Results and Discussion

This section evaluates through offline simulation whether the mean biological gait descriptors reported in Table 1 can be reproduced by the designed CPG networks. Kuramoto and Hopf are evaluated independently under unidirectional and bidirectional

communication using their respective MRGS-selected parameters. All reported CPG errors are calculated relative to the mean biological targets, while between-specimen standard deviations are used only to provide biological context. The results describe computational oscillator-network behavior and do not constitute physical-robot validation.

4.1. Kuramoto Network Performance

The Kuramoto implementation is evaluated as a phase-centered network in which the output amplitude is prescribed directly and coordination is regulated through phase coupling. Its performance is therefore expected to depend mainly on synchronization accuracy rather than on amplitude adaptation. The discussion follows the temporal trajectories, amplitude fidelity, phase-offset convergence, synchronization time, and dominant-frequency behavior.

4.1.1. Temporal and Amplitude Response

The Kuramoto temporal response is shown in Figure 7. Panel A presents the within-pair PM–CPD trajectories, whereas Panel B shows the coordination among the four PM oscillators. Under both communication schemes, the network rapidly establishes the prescribed inter-limb and within-pair phase relationships. Because the output amplitude is imposed directly, synchronization corrections appear mainly as abrupt changes in angular slope rather than through gradual amplitude adaptation.

The initial transient is more hierarchical under unidirectional coupling, whereas reciprocal corrections distribute the adjustment across the network under bidirectional coupling. In a physical implementation, these rapid startup corrections could impose high actuator-rate or torque demands; phase-consistent initialization or gradual command activation would therefore be appropriate mitigation strategies.

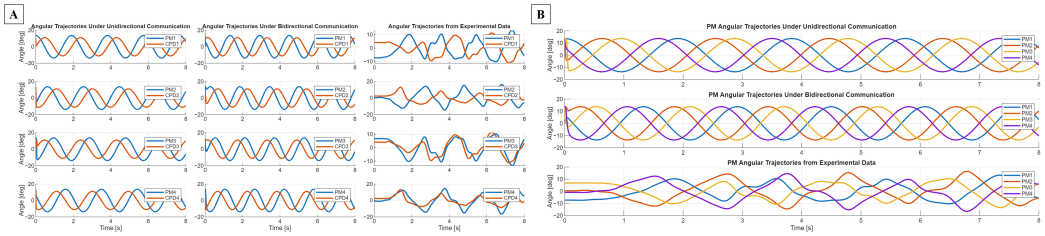


Figure 7. Kuramoto model temporal response: (**A**) within-pair angular trajectories of each PM oscillator and its corresponding CPD oscillator; (**B**) angular trajectories of the PM oscillators (PM1–PM4).

The amplitude behavior in Table 2 follows directly from the output definition $x_i = A_i \cos(\theta_i)$. The prescribed envelope is therefore reproduced almost exactly: the maximum PM error is 0.0007%, while the CPD error is either zero or reaches 0.0009% for CPD4 under unidirectional communication. These values verify the numerical accuracy of the output scaling, but they do not demonstrate intrinsic amplitude regulation or robustness to actuator loading. Unlike the Hopf amplitude results, which quantify how coupling perturbs a dynamic limit cycle, the Kuramoto values mainly confirm that the commanded stroke is fixed by construction. This provides predictable joint excursions, but it also means that the model has no internal amplitude state with which to soften startup, adapt stride magnitude, or absorb coupling-induced transients.

Table 2. Kuramoto model: output amplitudes (half peak-to-peak) and percent errors relative to the adopted target amplitudes ($A_{\mathrm{PM}} = 13.7°$, $A_{\mathrm{CPD}} = 11.1°$). Best-performing values are highlighted in bold.

Oscillator	Unidirectional [deg]	$\lvert e_A \rvert$ [%]	Bidirectional [deg]	$\lvert e_A \rvert$ [%]
PM1	13.6999	0.0007	**13.7000**	**0.0000**
PM2	**13.7000**	**0.0000**	13.6999	0.0007
PM3	**13.7000**	**0.0000**	**13.7000**	**0.0000**
PM4	**13.6999**	**0.0007**	**13.6999**	**0.0007**
CPD1	**11.1000**	**0.0000**	**11.1000**	**0.0000**
CPD2	**11.1000**	**0.0000**	**11.1000**	**0.0000**
CPD3	**11.1000**	**0.0000**	**11.1000**	**0.0000**
CPD4	11.0999	0.0009	**11.1000**	**0.0000**

4.1.2. Phase-Coordination Response

The transient phase behavior is shown in Figure 8. Panels A and B present the PM offsets relative to PM1, whereas Panels C and D show the corresponding within-pair PM–CPD offsets for unidirectional and bidirectional communication, respectively. Both configurations converge toward the prescribed phase relations. The unidirectional network exhibits predominantly monotonic convergence, although the PM3–CPD3 relation shows a temporary overshoot, whereas reciprocal coupling produces smaller non-monotonic corrections across a broader set of phase relations.

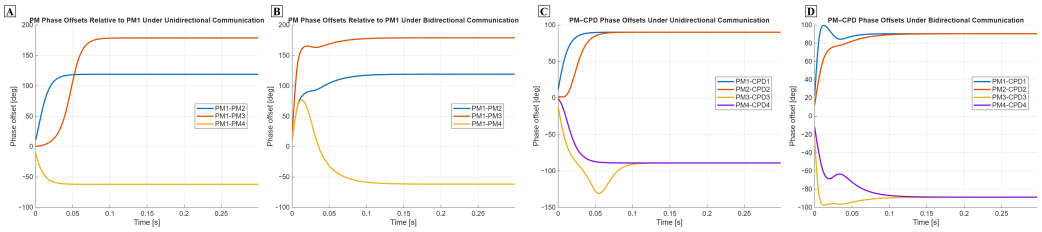


Figure 8. Kuramoto model phase-coordination response: (**A**) PM phase offsets relative to PM1 under unidirectional communication; (**B**) PM phase offsets relative to PM1 under bidirectional communication; (**C**) within-pair PM–CPD phase offsets under unidirectional communication; (**D**) within-pair PM–CPD phase offsets under bidirectional communication.

The mean phase-offset values reported in Table 3 show that both communication schemes reproduce the adopted mean coordination pattern with high precision. The unidirectional errors remain below 1% for all offsets, ranging from 0.21% to 0.61% for the PM relations and from 0.42% to 0.43% for the PM–CPD relations. Bidirectional coupling further reduces the steady-state phase error, with PM-offset errors between 0.07% and 0.16% and PM–CPD errors between 0.05% and 0.07%. This improvement suggests that reciprocal coupling distributes phase corrections more evenly across the network, which enhances final phase accuracy even though it can introduce slightly more complex transient behavior.

For the directly measured phase descriptors, the Kuramoto errors can be interpreted relative to the between-specimen standard deviations in Table 1. In the unidirectional network, the absolute deviations for the same-side and opposite-side merus phases are approximately 0.376°, which are within or approximately equal to their biological dispersions of 0.45° and 0.38°. The pulling and pushing deviations are approximately 0.376°–0.379°, slightly exceeding their corresponding standard deviations of 0.23° and 0.31°. In the bidirectional network, the directly matched phase deviations range from approximately 0.048° to 0.122° and remain below the corresponding biological standard deviations. The composite

PM1–PM4 relation is not included in this direct comparison because its target combines phase descriptors rather than representing a separately reported biological measurement.

Table 3. Kuramoto model: mean phase offsets after convergence and percent errors relative to the adopted mean biological phase targets. For offsets reported as negative, the target is shown using both equivalent angle conventions: positive-angle and wrapped negative forms. Best-performing values are highlighted in bold.

Phase Offset	Unidirectional [deg]	$\lvert e_\phi \rvert$ [%]	Bidirectional [deg]	$\lvert e_\phi \rvert$ [%]	Target [deg]
PM1–PM2	118.924	0.32	**119.178**	**0.10**	119.300
PM1–PM3	178.724	0.21	**178.980**	**0.07**	179.100
PM1–PM4	−61.976	0.61	**−61.698**	**0.16**	298.400/−61.600
PM1–CPD1	90.124	0.42	**90.443**	**0.06**	90.500
PM2–CPD2	90.124	0.42	**90.438**	**0.07**	90.500
PM3–CPD3	−89.079	0.43	**−88.760**	**0.07**	271.300/−88.700
PM4–CPD4	−89.076	0.42	**−88.748**	**0.05**	271.300/−88.700

4.1.3. Convergence and Frequency Response

The unidirectional and bidirectional Kuramoto networks both satisfied the phase-convergence criterion at 0.098 s, corresponding to approximately 0.051 gait cycles. Both therefore established the prescribed coordination within a small fraction of the target period, $T \approx 1.916$ s. Both configurations also preserved the prescribed cadence: the unidirectional network produced $f_{\text{dom}} = 0.5217$ Hz, with an absolute error of 0.0003 Hz (0.06%), whereas the bidirectional network produced $f_{\text{dom}} = 0.5220$ Hz, with no measurable error at the reported precision (0.00%).

4.2. Hopf Network Performance

The computational Hopf implementation is evaluated as a limit-cycle formulation in which phase coordination and amplitude regulation are coupled. The oscillator must approach its stable orbit before the output reaches its steady rhythmic amplitude. For that reason, the simulated response is expected to show a visible amplitude-growth transient and possible amplitude deviations introduced by coupling before reaching steady rhythmic behavior.

4.2.1. Temporal and Amplitude Response

The Hopf temporal response is shown in Figure 9. Panel A presents the within-pair PM–CPD trajectories, whereas Panel B shows the PM coordination. In both communication schemes, the oscillations develop gradually from the initial condition as the limit-cycle amplitude and phase relationships are established simultaneously. The selected unidirectional configuration reaches coordinated motion more rapidly, whereas the bidirectional configuration exhibits a slower transient because the two networks use different MRGS-selected (R, ϵ) parameter sets.

Unlike the immediate full-amplitude corrections observed with Kuramoto, the Hopf dynamics provide a gradual rhythmic onset. This may reduce abrupt command changes in a physical implementation, although the initial cycles do not yet exhibit the final stride amplitude or phase timing.

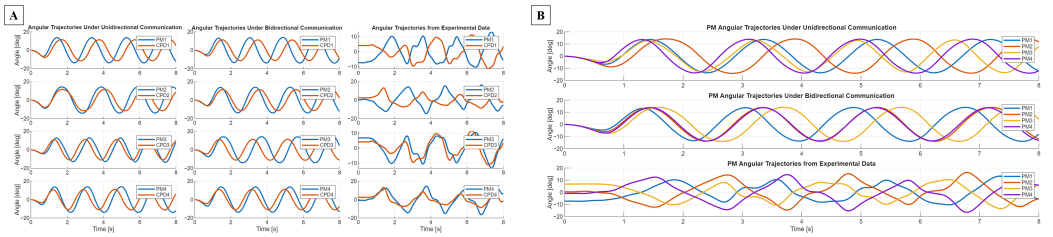


Figure 9. Hopf model temporal response: (**A**) within-pair angular trajectories of each PM oscillator and its corresponding CPD oscillator; (**B**) angular trajectories of the PM oscillators (PM1–PM4).

The amplitude values in Table 4 reflect the balance between radial restoration and coupling. The unidirectional configuration combines the smaller radius $R = 1.83$ with the larger gain $\epsilon = 1.19$. PM1, which acts as the upstream reference, remains close to the target with an error of 0.16%, whereas the coupled downstream PM and CPD units reach errors of approximately 3.20–3.34%, producing a network mean of 2.87%. The stronger interaction accelerates phase transmission but also perturbs the Cartesian state away from its uncoupled radius. By comparison, the bidirectional configuration uses a larger radius $R = 2.86$ and a smaller gain $\epsilon = 0.55$, reducing the coupling disturbance relative to the radial dynamics; PM and CPD errors then remain within 0.26–0.42%, with a network mean of 0.32%. The improved amplitude preservation is therefore a property of the complete selected parameter–topology combination, not of communication direction alone. Mechanistically, the selected solutions reveal a trade-off: stronger relative coupling favors rapid phase correction, whereas a larger radial scale and weaker coupling better preserve the intended limit-cycle magnitude.

Table 4. Hopf model: output amplitudes (half peak-to-peak) and percent errors relative to the adopted target amplitudes ($A_{\mathrm{PM}} = 13.7°$, $A_{\mathrm{CPD}} = 11.1°$). Best-performing values are highlighted in bold.

Oscillator	Unidirectional [deg]	$\lvert e_A \rvert$ [%]	Bidirectional [deg]	$\lvert e_A \rvert$ [%]
PM1	**13.7220**	**0.16**	13.7578	0.42
PM2	14.1382	3.20	**13.7470**	**0.34**
PM3	14.1382	3.20	**13.7554**	**0.40**
PM4	14.1382	3.20	**13.7465**	**0.34**
CPD1	11.4550	3.20	**11.1285**	**0.26**
CPD2	11.4706	3.34	**11.1300**	**0.27**
CPD3	11.4700	3.33	**11.1297**	**0.27**
CPD4	11.4700	3.33	**11.1291**	**0.26**

When interpreted against the measured biological amplitude variability, all simulated amplitude deviations remain within the observed between-specimen dispersion. The Kuramoto discrepancies are at most 0.0001°, whereas the largest Hopf deviations from the mean targets are 0.4382° for PM and 0.3706° for CPD. These values remain below the corresponding biological standard deviations of 1.8° and 1.6°. This comparison provides biological context for the simulated errors, although it does not imply that the controller outputs reproduce the full specimen-level amplitude distribution.

4.2.2. Phase-Coordination Response

The Hopf phase response is shown in Figure 10. Panels A and B present the PM offsets relative to PM1, while Panels C and D show the within-pair PM–CPD relations for unidirectional and bidirectional communication, respectively. The phase relations approach their prescribed values but retain bounded oscillations after convergence. This behavior

results from the Cartesian coupling in Equation (11), where phase corrections can also perturb the radial state and produce repeated amplitude–phase interactions.

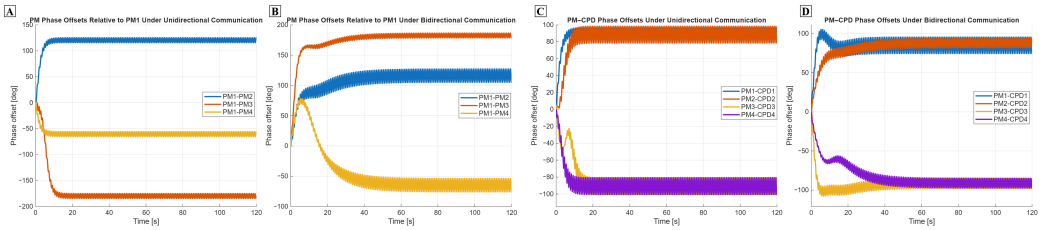


Figure 10. Hopf model phase-coordination response: (**A**) PM phase offsets relative to PM1 under unidirectional communication; (**B**) PM phase offsets relative to PM1 under bidirectional communication; (**C**) within-pair PM–CPD phase offsets under unidirectional communication; (**D**) within-pair PM–CPD phase offsets under bidirectional communication.

The magnitude of these residual oscillations is quantified in Table 5. The relative residual amplitude is defined as $A_{\text{res,rel}} = 100A_{\text{res}}/|\phi_{\text{target}}|$, where ϕ_{target} is expressed in the interval $[-180°, 180°]$. Consequently, the largest angular oscillation does not necessarily produce the largest relative residual amplitude. In the selected unidirectional configuration, the residual oscillation amplitudes range from 4.800° to 9.899°, with relative residual amplitudes between 2.68% and 11.15%. In the bidirectional configuration, they range from 5.087° to 13.577°, with relative residual amplitudes between 2.84% and 22.04%. The largest angular oscillation corresponds to approximately 72 ms of timing variation at 0.522 Hz. In a future physical robot, this instantaneous variation could potentially shift the beginning or end of support, propulsion, and recovery motions. Consequently, a low simulated mean phase error would not by itself guarantee repeatable physical foot contacts. The bidirectional parameter–topology combination reduces downstream PM–CPD residuals in some branches, but increases the sensitivity of reference-adjacent relations such as PM1–PM2, PM1–PM4, and PM1–CPD1.

Table 5. Hopf model: residual oscillations in phase offsets after convergence, reported as half peak-to-peak amplitude A_{res} and relative residual amplitude $A_{\text{res,rel}}$. Best-performing values are highlighted in bold.

Phase Offset	Unidirectional A_{res} [deg]	$A_{\text{res,rel}}$ [%]	Bidirectional A_{res} [deg]	$A_{\text{res,rel}}$ [%]
PM1–PM2	**4.800**	**4.02**	13.192	11.06
PM1–PM3	**4.800**	**2.68**	5.087	2.84
PM1–PM4	**4.800**	**7.79**	13.577	22.04
PM1–CPD1	**4.800**	**5.30**	11.862	13.11
PM2–CPD2	9.899	10.94	**7.298**	**8.06**
PM3–CPD3	9.893	11.15	**7.556**	**8.52**
PM4–CPD4	9.892	11.15	**7.503**	**8.46**

The mean phase-offset errors in Table 6 indicate that the Hopf network reproduces the adopted mean coordination pattern with configuration-dependent precision. In the selected unidirectional configuration, the errors remain between 0.78% and 2.27%, with a mean of 1.79%. In the selected bidirectional configuration, the range increases to 1.50–6.68%, with a mean of 4.00%, and every reported offset shows a larger mean error. However, these averages must be interpreted together with the residual envelopes in Table 5: a relation can have an acceptable mean while still crossing a wider range of instantaneous phase values. The selected bidirectional parameters therefore favor preservation of the radial amplitude, whereas the unidirectional parameters favor both a more accurate mean phase pattern and smaller oscillations in several reference-adjacent relations.

Table 6. Hopf model: Mean phase offsets after convergence and percent errors relative to the adopted mean biological phase targets. Equivalent positive-angle and wrapped negative forms are shown for offsets near the angular boundary or represented as negative values in the trajectories. Errors are computed using the minimum circular difference. Best-performing values are highlighted in bold.

Phase Offset	Unidirectional [deg]	$\lvert e_\phi \rvert$ [%]	Bidirectional [deg]	$\lvert e_\phi \rvert$ [%]	Target [deg]
PM1–PM2	**120.689**	**1.16**	115.522	3.17	119.300
PM1–PM3	**180.489/−179.511**	**0.78**	181.788/−178.212	1.50	179.100/−180.900
PM1–PM4	**−60.211**	**2.25**	−65.019	5.55	298.400/−61.600
PM1–CPD1	**91.891**	**1.54**	84.458	6.68	90.500
PM2–CPD2	**88.456**	**2.26**	87.114	3.74	90.500
PM3–CPD3	**−90.710**	**2.27**	−92.153	3.89	271.300/−88.700
PM4–CPD4	**−90.709**	**2.26**	−91.758	3.45	271.300/−88.700

Relative to the biological phase variability, the Hopf mean-offset deviations are larger than those of Kuramoto. For the directly matched descriptors, the unidirectional Hopf deviations range from approximately 1.389° to 2.044°, corresponding to about 3.1–8.9 times the associated between-specimen standard deviations. The bidirectional deviations range from approximately 2.688° to 6.042°, or about 7.1–26.3 times the corresponding standard deviations. The residual oscillation amplitudes of 4.800°–13.577° are also substantially larger than the measured phase dispersions of 0.23°–0.45°. Thus, the phase differences between the simulated configurations are not small relative to the biological variability observed in the four specimens, particularly for the Hopf networks. As with the Kuramoto comparison, the composite PM1–PM4 target is excluded from the direct standard-deviation comparison.

4.2.3. Convergence and Frequency Response

The unidirectional and bidirectional Hopf networks converged in 16.070 and 39.792 s, corresponding to approximately 8.4 and 20.8 gait cycles, respectively. Thus, the selected unidirectional configuration establishes the prescribed coordination substantially faster, although both Hopf configurations converge much more slowly than Kuramoto. The target cadence is nevertheless preserved: the unidirectional network produced $f_{\mathrm{dom}} = 0.52211$ Hz, with an absolute error of 0.00011 Hz (0.02%), whereas the bidirectional network produced 0.52206 Hz, with an absolute error of 0.00006 Hz (0.01%). The main limitation of the selected Hopf configurations is therefore their coordination transient and residual phase motion rather than frequency generation.

4.3. Comparison of the Implemented Kuramoto and Hopf Formulations

The implemented Kuramoto and Hopf networks reproduced the prescribed gait coordination through different dynamic mechanisms. The phase-only Kuramoto formulation provided rapid synchronization, negligible error in the prescribed output amplitudes, and high phase accuracy while preserving the target frequency. In contrast, the Hopf formulation generated a gradual limit-cycle onset and internal amplitude dynamics, but required substantially longer coordination transients and retained bounded phase oscillations after convergence. Within the Hopf configurations, stronger relative coupling in the unidirectional network improved phase convergence at the expense of amplitude preservation, whereas the bidirectional configuration better preserved amplitude but converged more slowly and exhibited larger residual phase motion.

A sensitivity analysis evaluated ten configurations for each Kuramoto communication scheme. Relative to the reference configuration in Section 3.5, one condition was varied at a time: the upper gain bound, phase-error tolerance, integration time step, or nominal persistence setting. An additional exploratory objective selected the minimum coupling

gain satisfying $t_c \leq 1/f$, corresponding to phase-band entry within one biological period ($1/f \approx 1.916$ s). The biological targets, topology matrices, initial phases, and 8 s simulation horizon remained fixed. Table 7 summarizes the selected gains and phase-convergence times.

The selected coupling gains and transient times depended on the search domain and selection criterion. Minimizing phase-convergence time favored gains near the upper search bound, whereas the minimum-gain objective produced substantially smaller gains with longer transients. The reference final refinement grids contained 12 unidirectional and 13 bidirectional candidates sharing the same minimum sampled time, demonstrating that the reported gain precision does not identify a unique optimum. Changing the phase tolerance or integration step also altered the relative timing of the two communication schemes, while the tested persistence settings left the selections unchanged. Across all twenty scenarios, the phase-error band was retained after entry until the end of the simulation. Frequency estimates obtained from phase slopes over the final 4 s remained approximately 0.522 Hz. These results support consistent coordination under the tested conditions, while showing that exact gains and small timing differences between communication schemes depend on the search and numerical settings. Comparisons with Hopf remain conditional on the specific Hopf configurations reported in this study.

Table 7. Sensitivity of the selected Kuramoto coupling gains and phase-convergence times. Each variant changes one condition relative to the reference configuration.

Setting	$\omega_{\mathbf{uni}}$	$t_{c,\mathbf{uni}}$ (s)	$\omega_{\mathbf{bi}}$	$t_{c,\mathbf{bi}}$ (s)
Reference	99.29	0.098	99.28	0.098
$\omega_{\max} = 50$	49.88	0.194	49.65	0.198
$\omega_{\max} = 150$	148.09	0.066	145.98	0.066
$\delta = 2.5°$	98.92	0.106	98.85	0.116
$\delta = 10°$	99.35	0.090	97.62	0.082
$\Delta t = 0.001$ s	99.76	0.097	99.29	0.099
$\Delta t = 0.0005$ s	99.97	0.0965	99.79	0.099
$\tau_h = 0.025$ s	99.29	0.098	99.28	0.098
$\tau_h = 0.100$ s	99.29	0.098	99.28	0.098
Minimum-gain objective	5.03	1.914	5.19	1.912

Table 8 shows that both Kuramoto configurations satisfied the phase-band criterion in all sampled trials and retained the band until the end of the simulation. The unidirectional Hopf configuration satisfied the first-entry criterion in all 150 randomized trials. The bidirectional Hopf configuration satisfied it in 49 of 150 trials: 16/50 with local phase variations, 16/50 with wider phase variations, and 17/50 with wider phase and radius variations. The remaining 101 trials did not satisfy the criterion within 120 s. All simulated trajectories remained finite over the evaluated horizon.

Despite the variation in first-entry times and criterion attainment, the late-window Hopf diagnostics remained close to their respective nominal values. Across the randomized Hopf trials, the maximum change in mean absolute phase error was below 0.030°, the maximum change in mean phase-slope frequency was below 7.5×10^{-6} Hz, and the maximum change in mean amplitude error was below 3.8×10^{-5} percentage points. Both Hopf configurations exhibited phase-band exits after their first qualifying entry, including in the nominal trials, consistent with their persistent phase oscillations. These observations distinguish sensitivity of the first-entry criterion from variation in the late oscillatory response. The all-zero Hopf initialization remained at equilibrium without generating oscillations. The findings are restricted to the tested initialization sets and finite simulation horizon.

Table 8. Response to varied, nonzero initial conditions with fixed network parameters. Counts include all randomized trials; time statistics include only trials satisfying the phase-band criterion within 120 s. Nominal trials and all-zero Hopf diagnostics are excluded.

Network	Criterion Met	Median t_c (s)	Range (s)
Kuramoto uni	100/100	0.066	0.038–0.108
Kuramoto bi	100/100	0.090	0.038–0.134
Hopf uni	150/150	11.661	6.840–28.252
Hopf bi	49/150	31.470	15.474–51.256

These differences provide implementation-oriented criteria for model selection rather than establishing a universally superior oscillator family. The implemented Kuramoto formulation is better suited to applications in which low computational complexity, rapid phase coordination, and prescribed joint amplitudes are priorities, although its abrupt synchronization transient may require command smoothing in a physical system. The implemented Hopf formulation is more appropriate when gradual rhythmic emergence and intrinsic amplitude dynamics are desired, provided that longer synchronization times and residual phase variations can be accommodated. These observations apply only to the specific formulations, parameterizations, and communication topologies evaluated in this study and require physical-robot validation.

5. Conclusions

This study developed a traceable pipeline for translating measured biological locomotion into an executable CPG network specification. Applied to the walking gait of *Uca pugnax*, the procedure converted measured frequency, amplitude, and phase descriptors into an eight-oscillator architecture comprising four independent PM units and four dependent CPD units, with explicit coupling topology, phase targets, and communication direction. The resulting specification provides a reproducible link between biological gait analysis and computational CPG implementation.

Both evaluated oscillator formulations reproduced the prescribed cadence and coordination under offline simulation, but through different mechanisms. The phase-only Kuramoto implementation provided rapid synchronization and high phase accuracy with amplitudes fixed by construction. The Hopf implementation generated gradual limit-cycle growth and internal amplitude dynamics, while exhibiting longer convergence times and bounded residual phase oscillations. Its selected parameter sets further revealed a trade-off between phase correction and amplitude preservation.

The comparison therefore demonstrates how the proposed pipeline can support CPG model selection using measurable implementation criteria. For the implemented networks, Kuramoto should be preferred when high phase accuracy, rapid synchronization, and externally prescribed joint amplitudes are priorities. Hopf should be preferred when gradual rhythmic onset and intrinsic amplitude dynamics are desired, provided that longer convergence times and bounded residual phase oscillations can be accommodated. These guidelines apply to the specific Kuramoto and Hopf formulations, topologies, parameter domains, and mean biological targets evaluated in this study.

The present validation remains computational and covers the specified initial-condition sets. Future work will evaluate the networks on the physical robotic platform, incorporating actuator dynamics, foot–terrain interaction, sensory feedback, adaptive gait modulation, and broader parameter-search strategies. Disturbance rejection will be assessed through explicit external-load and contact-change scenarios, measuring recovery of rhythmic output and gait coordination. These experiments will determine whether the simulated network behavior translates into stable robotic locomotion.

Author Contributions: Investigation, D.A.-V.; methodology, D.A.-V., R.C., J.I., S.D.G. and R.B.-B.; formal analysis, D.A.-V., J.I. and R.B.-B.; writing—original draft preparation, D.A.-V.; writing—review and editing, R.C., J.I., S.D.G. and R.B.-B.; supervision, R.C., J.I., S.D.G. and R.B.-B. All authors have read and agreed to the published version of the manuscript.

Funding: Daniel Alberto Arriaga Ventura acknowledges doctoral scholarship support from the Secretaría de Ciencia, Humanidades, Tecnología e Innovación (SECIHTI), Mexico, and from the Instituto Tecnológico y de Estudios Superiores de Monterrey through the Beca Institucional Programas Científicos Doctorado.

Institutional Review Board Statement: Institutional animal ethics review was not sought for this study. This decision was based on the authors' interpretation of the taxonomic scope specified in Clause 1.2 of Mexican Official Standard NOM-062-ZOO-1999, which does not include crustaceans among the listed animal groups. All *Uca pugnax* specimens were obtained from a captive breeder, without collection from the wild for this study. Live-animal procedures comprised handling and placement in the recording arena, and video recording of spontaneous locomotion. No live-animal surgery or euthanasia was performed, and no animals were sacrificed for this study. Specimens used for post-mortem biomechanical characterization had died naturally before their use. Animal care included access to moist and dry areas, a fine-sand substrate, hiding places, aquatic vegetation, water filtration, full-spectrum lighting, commercial aquatic flake food, and visual barriers intended to reduce external disturbance. Handling and recording sessions were limited in duration to minimize disturbance. Further husbandry details are provided in Section 3.3.

Data Availability Statement: The data supporting the findings of this study are available from the corresponding author upon reasonable request. Access to the data is subject to prior approval by all authors.

Acknowledgments: During the preparation and revision of this manuscript, ChatGPT (OpenAI; GPT-6.1 Sol, maximum reasoning setting) assisted with generating the experimental-setup schematic in Figure 4A, improving the coherence of the manuscript text, and refining the table formatting. Grammarly was used for English-language editing. The authors reviewed and edited the assisted material and take full responsibility for the final content of this publication.

Conflicts of Interest: The authors declare no conflicts of interest.

Abbreviations

The following abbreviations are used in this manuscript:

CPG	Central Pattern Generator
CPD	Carpus–propodus–dactylus
FFT	Fast Fourier Transform
MRGS	Multi-resolution grid search
PM	Pair of Merus

References

1. Du Plessis, A.; Broeckhoven, C.; Yadroitsava, I.; Yadroitsev, I.; Hands, C.H.; Kunju, R.; Bhate, D. Beautiful and Functional: A Review of Biomimetic Design in Additive Manufacturing. *Addit. Manuf.* **2019**, *27*, 408–427. [CrossRef]
2. Hashemi Farzaneh, H. Bio-Inspired Design: The Impact of Collaboration Between Engineers and Biologists on Analogical Transfer and Ideation. *Res. Eng. Des.* **2020**, *31*, 299–322. [CrossRef]
3. Ijspeert, A.J. Central Pattern Generators for Locomotion Control in Animals and Robots: A Review. *Neural Netw.* **2008**, *21*, 642–653. [CrossRef] [PubMed]
4. Yu, J.; Tan, M.; Chen, J.; Zhang, J. A Survey on CPG-Inspired Control Models and System Implementation. *IEEE Trans. Neural Netw. Learn. Syst.* **2014**, *25*, 441–456. [CrossRef] [PubMed]
5. Marder, E.; Bucher, D. Central Pattern Generators and the Control of Rhythmic Movements. *Curr. Biol.* **2001**, *11*, R986–R996. [CrossRef] [PubMed]
6. Crespi, A.; Badertscher, A.; Guignard, A.; Ijspeert, A.J. AmphiBot I: An Amphibious Snake-Like Robot. *Robot. Auton. Syst.* **2005**, *50*, 163–175. [CrossRef]

7. Ijspeert, A.J.; Crespi, A.; Ryczko, D.; Cabelguen, J.M. From Swimming to Walking with a Salamander Robot Driven by a Spinal Cord Model. *Science* **2007**, *315*, 1416–1420. [CrossRef] [PubMed]
8. Crespi, A.; Karakasiliotis, K.; Guignard, A.; Ijspeert, A.J. Salamandra Robotica II: An Amphibious Robot to Study Salamander-Like Swimming and Walking Gaits. *IEEE Trans. Robot.* **2013**, *29*, 308–320. [CrossRef]
9. Zhou, C.; Low, K.H. Kinematic Modeling Framework for Biomimetic Undulatory Fin Motion Based on Coupled Nonlinear Oscillators. In Proceedings of the 2010 IEEE/RSJ International Conference on Intelligent Robots and Systems, Taipei, Taiwan, 18–22 October 2010; pp. 934–939. [CrossRef]
10. Yu, J.; Tan, M. CPG-Based Swimming Control. In *Motion Control of Biomimetic Swimming Robots*; Research on Intelligent Manufacturing; Springer: Berlin/Heidelberg, Germany, 2020; Chapter 4, pp. 71–99. [CrossRef]
11. Jouaiti, M.; Hénaff, P. Comparative Study of Forced Oscillators for the Adaptive Generation of Rhythmic Movements in Robot Controllers. *Biol. Cybern.* **2019**, *113*, 547–560. [CrossRef] [PubMed]
12. Morantes, G.; Cappelletto, J.; Fernandez, G.; Clotet, R.; Torrealba, R.; Guerrero, S. Comparison of CPG Topologies for Bipedal Gait. In Proceedings of the 2016 IEEE Ecuador Technical Chapters Meeting (ETCM), Guayaquil, Ecuador, 12–14 October 2016; pp. 1–6. [CrossRef]
13. Cayetano-Jiménez, I.U.; Arriaga-Ventura, D.; Martinez-Ríos, E.A.; Bustamante-Bello, R. Van der Pol Oscillators and Phase-Locked Loops: A Transparent Model for Central Pattern Generators in Bioinspired Robotics. *IEEE Access* **2024**, *12*, 184071–184090. [CrossRef]
14. Almeida, J.F.; Santos, C.P. Bio-inspired control strategies in wearable robotics: A comprehensive review of CPGs and DMPs. *Annu. Rev. Control* **2025**, *60*, 100991. [CrossRef]
15. Acebrón, J.A.; Bonilla, L.L.; Pérez Vicente, C.J.; Ritort, F.; Spigler, R. The Kuramoto Model: A Simple Paradigm for Synchronization Phenomena. *Rev. Mod. Phys.* **2005**, *77*, 137–185. [CrossRef]
16. Li, X.; Shougat, M.R.E.U.; Mollik, T.; Beal, A.N.; Dean, R.N.; Perkins, E. Stochastic Effects on a Hopf Adaptive Frequency Oscillator. *J. Appl. Phys.* **2021**, *129*, 224901. [CrossRef]
17. Espinal, A.; Rostro-Gonzalez, H.; Carpio, M.; Guerra-Hernandez, E.I.; Ornelas-Rodriguez, M.; Sotelo-Figueroa, M. Design of Spiking Central Pattern Generators for Multiple Locomotion Gaits in Hexapod Robots by Christiansen Grammar Evolution. *Front. Neurorobot.* **2016**, *10*, 6. [CrossRef] [PubMed]
18. Li, G.; Ijspeert, A.; Hayashibe, M. AI-CPG: Adaptive Imitated Central Pattern Generators for Bipedal Locomotion Learned Through Reinforced Reflex Neural Networks. *IEEE Robot. Autom. Lett.* **2024**, *9*, 5190–5197. [CrossRef]
19. Sirisathitkul, C.; Glawtanong, P.; Eadkong, T.; Sirisathitkul, Y. Digital Video Analysis of Falling Objects in Air and Liquid Using Tracker. *Rev. Bras. Ensino Fís.* **2013**, *35*, 1504. [CrossRef]

Disclaimer/Publisher's Note: The statements, opinions and data contained in all publications are solely those of the individual author(s) and contributor(s) and not of MDPI and/or the editor(s). MDPI and/or the editor(s) disclaim responsibility for any injury to people or property resulting from any ideas, methods, instructions or products referred to in the content.